Research Article | Vol. 31, No. 22 / 23 Oct 2023 / Optics Express 37262
Optics EXPRESS

Multipass wide-field phase imager

ÁLVARO CUEVAS,[1,*] DANIEL TIEMANN,[1] ROBIN CAMPHAUSEN,[1] IRIS CUSINI,[1,2] ANTONIO PANZANI,[2] RAJDEEP MUKHERJEE,[1,3] FEDERICA VILLA,[2] AND VALERIO PRUNERI[1,4]

[1]*ICFO-Institut de Ciencies Fotoniques, The Barcelona Institute of Science and Technology, 08860 Castelldefels, Barcelona, Spain*
[2]*Politecnico di Milano, Dipartimento di Elettronica, Informazione e Bioingegneria, Piazza Leonardo da Vinci 32, 20133 Milano, Italy*
[3]*Karlsruhe Institute of Technology, 76131 Karlsruhe, Germany*
[4]*ICREA-Institució Catalana de Recerca i Estudis Avançats, Passeig Lluís Companys 23, 08010 Barcelona, Spain*
[*]*alvaro.cuevas@icfo.eu*

Abstract: Advances in optical imaging always look for an increase in sensitivity and resolution among other practicability aspects. Within the same scope, in this work we report a versatile interference contrast imaging technique, with high phase sensitivity and a large field-of-view of several mm^2. Sensitivity is increased through the use of a self-imaging non-resonant cavity, which causes photons to probe the sample in multiple rounds before being detected, where the configuration can be transmissive or reflective. Phase profiles can be resolved individually for each round thanks to a specially designed single-photon camera with time-of-flight capabilities and true pixels-off gating. Measurement noise is reduced by novel data processing combining the retrieved sample profiles from multiple rounds. Our protocol is especially useful under extremely low light conditions as required by biological or photo-sensitive samples. Results demonstrate more than a four-fold reduction in phase measurement noise, compared to single round imaging, and values close to the predicted sensitivity in case of the best possible cavity configuration, where all photons are maintained until n rounds. We also find good agreement with the theoretical predictions for low number of rounds, where experimental imperfections would play a minor role. The absence of a laser or cavity lock-in mechanism makes the technique an easy to use inspection tool.

1. Introduction

In optical metrology and sensing, the search for low noise data is a never ending task, which is ultimately limited by the Heisenberg uncertainty [1]. When using linear optics, sensitivity is bound by the inverse of the information resources available, $\Delta \propto \frac{1}{\sqrt{QM}}$, with Q entangled copies of M number of photons. Without quantum correlations ($Q = 1$) we obtain the *shot noise limit* [2]. Under such classical restriction, noise can only be reduced by increasing M arbitrarily. Unfortunately, this approach requires increasing the power, and represents a high risk for certain chemical bonds which degrade under strong illumination, not just in biological specimens [3–5], but also in synthetic compounds, for instance in the optical industry sector [6], among others. Alternatively, one can fix the number of photons which probe the sample, while allowing the photons to interact with the sample multiple (N) times, effectively providing a sensitivity bound that scales as $\Delta \propto \frac{1}{N}$. In this work, we opted for this second approach, while proposing a new protocol that combines the retrieved information from multiple light-sample interactions, biased on their relative "resource weight".

Inspection of low optical loss materials was a challenging task until the invention of differential interference contrast microscopy (DIM) in the 1960s [7]. With this technique two copies of

#499156 https://doi.org/10.1364/OE.499156
Journal © 2023 Received 4 Jul 2023; revised 28 Sep 2023; accepted 28 Sep 2023; published 20 Oct 2023

Optics EXPRESS

a coherent light beam are laterally displaced to traverse a target sample at different locations. When recombined later on, beams interfere according to their *optical path difference* (OPD), that can be defined as $OPD = l_1 n_1 - l_2 n_2$, with l_1 (l_2) and n_1 (n_2) the traveled distance and sample refractive index respectively, at location 1 (2). If both beams have no overlap when traversing the sample, or the phase is imprinted only in one beam, then the phase profile can be retrieved directly by *phase-shifting digital holography* (PSDH) [8,9]. Assuming an optical interference $I(x, y) = a + b\cos(c\phi(x, y) + d)$, this requires four interference measurements taken with four different phase offsets to find the parameters a, b, c, d, and $\phi(x, y) = \frac{2\pi OPD(x,y)}{\lambda}$. With partial beam overlapping, PSDH does not provide the phase profile directly, but a differential one that we call the *sheared phase* $\tilde{\phi}(x, y)$, which usually requires additional steps to be mapped into $\phi(x, y)$ as shown in [10] and [11]. These methods can be implemented only when the imaging system provides high spatial resolution.

During the last decade, DIM has been improved in different ways, comprising compactness [12], larger depth-of-field [13], and quantum light compatibility [14]. In this work, we take a step forward by combining our multi-pass approach based on a non-resonant cavity that keeps large amount of modes for high transversal resolution together with a non-scanning large field-of-view (FoV) DIM. To the best of our knowledge, multi-pass phase imaging has only been studied from the perspective of measurement on isolated rounds [15,16], while multi-pass fluorescence imaging has been studied in combination with active electro-optic control [17].

The requirements of our method are less restrictive than those of some modern microscopy techniques. For instance, it can analyse surface roughness or embedded structures in transparent samples, without the need of fluorescent labeling [18–21]. Let us suppose that the light dose is limited to a maximum power of M[photons/mm^2] by either the photo-sensitivity of the sample or the source power. When only letting pass once this amount of light through the sample, the phase noise scales like $\Delta\phi \propto \frac{1}{\sqrt{M}}$. If instead, M/N photons interact N times with the sample, the noise reduces to $\Delta\phi \propto \frac{1}{\sqrt{NM}}$ (additional information can be found in [22]). Reproducing this condition is especially challenging, because it requires a cavity which closes immediately after the light enters, and re-opens later for the output of any arbitrary Nth-round. Implementing such functionality by following the concept behind [23] would require a fast switching mirror, which has to change from transparent to reflective regime within fractions of a *ns*. Instead, we use a standard permanently open cavity and record all rounds that emerge from it per acquisition frame - not just the last accessible round. This is possible thanks to a specially designed time-of-flight resolving single-photon avalanche detector (SPAD) array camera, with true pixel-off gating capabilites. To date, cavity ring-down spectroscopy (CRDS) is the most sensitive technique which applies optical multi-pass [24,25]. Its working principle is based on quantifying the power decay rate of pulses leaking from the cavity in consecutive round trips. CRDS mainly reveals sample optical absorption and concentration, which can extend to spectral analysis only under resonance conditions, requiring locking mechanisms at laser and cavity levels. In principle it can provide OPD between two modes, but only when assisted by a spatially scanning method. Our method does not reach the CRDS sensitivity levels, but we are able to provide spatial and depth information of the target sample without the need of any scanning mechanism.

2. Theoretical model

Consider a system in which light is prepared in $|H\rangle = (|+\rangle + |-\rangle)/\sqrt{2}$ polarization. For every ray, a lateral displacer (LD) splits the components $|+\rangle$ and $|-\rangle$ by a shear distance d and parallel to the input trajectory. The two new rays then enter a non-resonant cavity, which has a partially reflective mirror M_R with reflectivity R at the entrance and a fully reflective one (M) at the opposite side. By utilizing a cavity round trip $\tau = 2L/c$, with length L, larger than the light source pulse width (Δt_p) and smaller than the pulse period (t_p), resonance is prevented. For

Optics EXPRESS

simplicity reasons, suppose also that the target sample is birefringent, so it adds a phase ϕ only in one of the two polarizations. Every time light leaks from the cavity, the output polarization can be described by $|\psi_n\rangle = (|+\rangle + e^{i\varphi^{(n)}}|-\rangle)/\sqrt{2}$ as shown in Fig. 1, with $\varphi_n = 2(n\phi + \alpha)$, while α is the phase offset added by the LD.

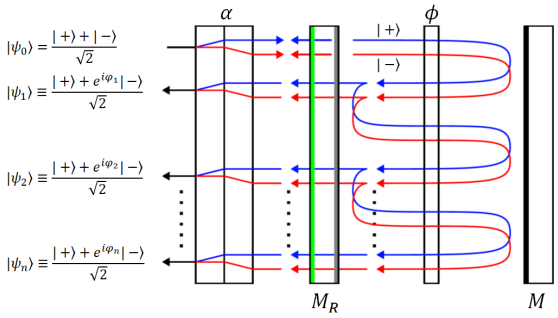

Fig. 1. Diagram of multi-pass DIM for every light ray. Input $|H\rangle$-polarized light is split into $|+\rangle$ (blue arrows) and $|-\rangle$ (red arrows) by a birefringent LD before reaching M_R, and reflects off M inside the cavity. Phases ϕ and α are only induced on $|-\rangle$. LD later recombines the outputs.

Due to the shear effect, an output beam in $\mathbf{r} = (x, y)$ coordinate will perceive an OPD between the $\mathbf{r}' = (x+\delta, y+\delta)$ and $\mathbf{r}'' = (x+\delta, y-\delta)$ locations inside the cavity for $|+\rangle$ and $|-\rangle$, respectively and with $\delta = d/\sqrt{2}$. Under those conditions, we can define the full output state as

$$|\Psi\rangle \approx R^{\frac{1}{2}}|\tau_0\rangle|\psi_0\rangle + \sum_{n=1}^{N}(1-R)(R\xi)^{\frac{n-1}{2}}|\tau_n\rangle|\psi_n\rangle \tag{1}$$

with

$$|\psi_n(\mathbf{r})\rangle = (|+(\mathbf{r})\rangle + e^{i2(n\tilde{\phi}(\mathbf{r})+\alpha)}|-(\mathbf{r})\rangle)/\sqrt{2} \tag{2}$$

and $\tilde{\phi}(\mathbf{r}) = \phi(\mathbf{r}'') - \phi(\mathbf{r}')$.

In Eq. (1) we introduce the N-dimensional temporal space that the system can resolve with $|\tau_n\rangle = |\tau_{n-1} + \tau\rangle$. The cavity losses are also included in the single-round optical efficiency parameter ξ, as well as the double pass factor at every round.

Utilizing PSDH on the system output allows us to retrieve the direct phase estimate

$$\hat{\theta}^{(n)} = \tan^{-1}\left[\frac{I_3^{(n)} - I_1^{(n)}}{I_0^{(n)} - I_2^{(n)}}\right], \tag{3}$$

and the target super-resolved phase estimate, $\hat{\phi}^{(n)} = \hat{\theta}^{(n)}/2n$ [22]. Here, the interference amplitudes are obtained by projecting the state into every round-time and the $|V\rangle$ polarization,

$$\begin{aligned} I_k^{(n)} &= |\langle\tau_n|\langle V|\Psi\rangle|^2 \\ &= \frac{\Gamma^{(n)}}{2}(1 + \mathcal{V}^{(n)}\cos(2(n\tilde{\phi} + \alpha_k))). \end{aligned} \tag{4}$$

The phase offsets are known and fixed to the values $\alpha_k = \frac{k\pi}{4}$ (with $k = [0, 3]$) by the observer, $\mathcal{V}^{(n)}$ is the interference visibility and $\Gamma^{(n)} = (R\xi)^{n-1}\Gamma^{(1)} = I_0^{(n)} + I_2^{(n)} = I_1^{(n)} + I_3^{(n)}$ is the interference amplitude. The formulation in Eq. (3) is equivalent to the one briefly described in the Introduction section, $I(x, y) = a + b(c\phi(x, y) + d)$, but more specific to our particular

Optics EXPRESS

case. Experimentally, each $I_k^{(n)}$ corresponds proportionally to the detected photon counts per acquisition, $I_k^{(n)} = p_k^{(n)}$. The uncertainty introduced by the PSDH can then be calculated by computing the standard deviation for the independent $p_k^{(n)}$ values through the partial derivatives formula, $\Delta O = \left(\sum_{k=0}^{3}\sum_{j=1}^{n}\left(\partial O/\partial p_k^{(j)}\cdot\Delta p_k^{(j)}\right)^2\right)^{1/2}$. From this calculation (see Supplement 1 for the derivation) we obtain

$$\Delta\hat{\phi}^{(n)} = \frac{1}{n\mathcal{V}^{(n)}\sqrt{2p^{(n)}}}, \tag{5}$$

where we have introduced the total number of photons detected per round, $p^{(n)} = \sum_{k=0}^{3} p_k^{(n)} = 2\Gamma^{(n)}$, while using the Poissonian standard deviation $\Delta p_k^{(n)} = \sqrt{p_k^{(n)}}$. This result is valid for any value of the shear δ, as long as it remains considerably small respect to the beam size, while the sample's optical efficiency is considered spatially homogeneous.

In order to obtain a more abrupt reduction in the phase noise, the next step is to study how phases from different rounds can contribute to it. Accordingly, we propose the following linear combination

$$\Phi^{(n)} = \sum_{m=1}^{n} w^{(m)}\hat{\phi}^{(m)}, \tag{6}$$

where weighting factors denote how many resources (interactions with the sample and how many photons) were detected to get each round phase estimate,

$$w^{(m)} = \frac{m^q p^{(m)}}{\sum_{i=1}^{m} i^q p^{(i)}}. \tag{7}$$

with q as an arbitrary exponent. The propagated noise from this new method (see Supplement 1 for derivation) will then correspond to

$$\Delta\Phi^{(n)} = \frac{\sqrt{\sum_{j=1}^{n}\frac{j^{2(q-1)}(R\xi)^{j-1}}{(\mathcal{V}^{(j)})^2}}}{\sqrt{2p^{(1)}}\sum_{m=1}^{n} m^q(R\xi)^{m-1}}. \tag{8}$$

This result is valid for any value of the shear δ, under the same assumptions considered for the calculation of $\Delta\hat{\phi}^{(n)}$.

In order to properly evaluate the noise of the multi-pass PSDH, Eq. (8) already includes a fixed number of total photons detected among all four phase offset acquisitions. This condition is imposed by the following normalization:

$$p^{(1)} \longrightarrow p'^{(1)} = p^{(1)}\cdot\frac{p^{(1)}}{\sum_{k=1}^{n} p^{(k)}} = \frac{p^{(1)}}{\sum_{k=1}^{n}(R\xi)^{k-1}}. \tag{9}$$

We then define the error scaling of $\hat{\phi}^{(n)}$ and $\Phi^{(n)}$ as:

$$\begin{aligned} S &= \frac{\Delta\hat{\phi}^{(n)}}{\Delta\hat{\phi}^{(1)}} = \frac{\mathcal{V}^{(1)}}{n\mathcal{V}^{(n)}(R\xi)^{\frac{n-1}{2}}}, \\ S' &= \frac{\Delta\Phi^{(n)}}{\Delta\Phi^{(1)}} = \frac{\mathcal{V}^{(1)}}{\sum_{m=1}^{n} m^q(R\xi)^{m-1}}\sqrt{\sum_{j=1}^{n}\frac{j^{2(q-1)}(R\xi)^{j-1}}{(\mathcal{V}^{(j)})^2}}, \end{aligned} \tag{10}$$

where $\Delta\hat{\phi}^{(1)} = \Delta\Phi^{(1)} = \frac{1}{\mathcal{V}^{(1)}\sqrt{2p^{(1)}}}$.

Optics EXPRESS

If we assume all light is preserved until the nth round, the exponent in the denominator of S becomes $\frac{n-1}{2} = 0$. We define this case as "all light at last round", which is determined by

$$S'' = \frac{\mathcal{V}^{(1)}}{n\mathcal{V}^{(n)}}, \tag{11}$$

We compare the noise scaling of Eqs. (10) and Eq. (11) in Fig. 2, showing that our method can reduce by at least five times the phase noise by combining only 5 rounds, and without increasing the number of photons detected.

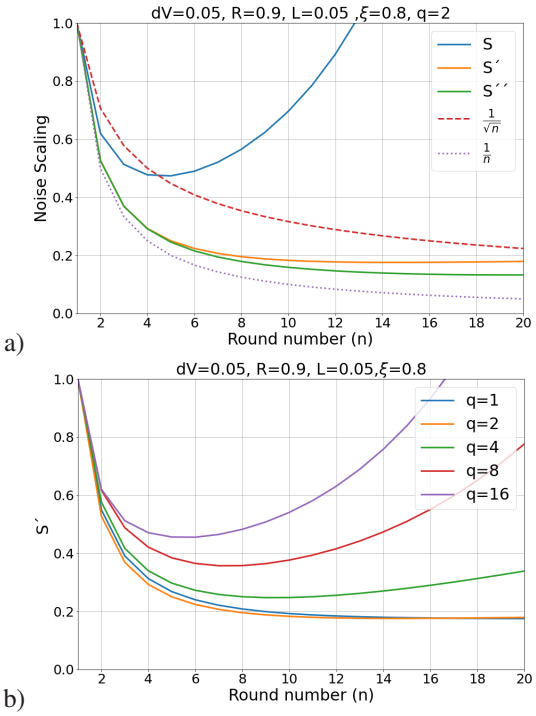

Fig. 2. Noise scaling simulation. a) Comparison between PSDH methods. S' outperforms S using realistic optical parameters, while it approaches to S'', in which photons do not leak from the cavity until round n. For the full round trip, we considered an efficiency $\xi = (1 - L)\xi_{cav}$, with $L = 1 - R - T$ being the partially reflective mirror losses and ξ_{cav} the efficiency of all other optical components within the cavity. We assume an interference visibility that scales like $\mathcal{V}^{(n)} = ((1 - dV)/1)^{n-1}$. Curves $1/\sqrt{n}$ and $1/n$ are only used as references, not respect to the shot noise limit. b) Comparison of S' for different values of q, where the larger its value, the higher the phase and noise contribution from high rounds number n.

3. Experimental implementation

3.1. Optical apparatus

We utilized a 840nm Vertical Cavity Surface Emitting Laser (VCSEL) as the light probe with a tunable pulse period of t_p>50μs and standard deviation width of Δt_p = 200ps. This source is first coupled into a single-mode fiber (SMF), then collimated with a $1/e^2$-diameter of D = 4mm and prepared in $|H\rangle$-polarization by a polarizing beam splitter (PBS). A quarter-wave plate (QWP) and a half-wave plate (HWP) are used before the PBS for controlling the optical power. The

Optics EXPRESS

LD-operation is implemented by a Savart plate (SP) of 10mm thickness, placed with a $\pi/4$-radian rotation in the x/y plane to induce a shear of $d = 450\mu$m. The SP is additionally tilted along the pitch axis with a motorized stage to further control the α parameter. Transparent samples can be placed immediately behind the partially reflective mirror (M_R) or immediately in front of the fully reflective mirror (M). In case of a reflective sample, M has to be replaced by the sample itself. For a proof of concept, we have chosen $R = 0.9$, and a fully variable reflective sample, by utilizing a spatial light modulator (SLM) with $R_{SLM} = 0.85$ at 840nm and placed with a $\pi/4$-radian rotation to match the $|+\rangle$ and $|-\rangle$ axes. The cavity optical efficiency is estimated as $\xi_{cav} = R_{SLM}(\xi_{optics}) \approx 0.8$, with $R_{SLM} \approx 0.88$ and ξ_{optics} the combined optical efficiency of all lenses and additional components.

Figure 3 shows the setup, where the cavity has a length $L = 1000$mm, providing the non-resonance condition $\Delta t_p < \tau < t_p$. Two lenses with focal length $F_c = 250$ mm are placed in a 4F telescope configuration between M_R and SLM. The optical interference of Eq. (4) is obtained from the secondary entrance of the system PBS, where output $|V\rangle$ polarization is reflected towards a camera sensor. In this arm, two more lenses with $F_1 = 200$mm and $F_2 = 300$mm are placed in 4F to image a 1.5× magnified replica of the sample plane into the camera sensor. One pinhole is placed between the two F_c lenses and another one between F_1 and F_2 lenses, both for removing scattered light. A 10nm bandpass filter (BPF) is placed in front of the SPAD camera to remove environmental light.

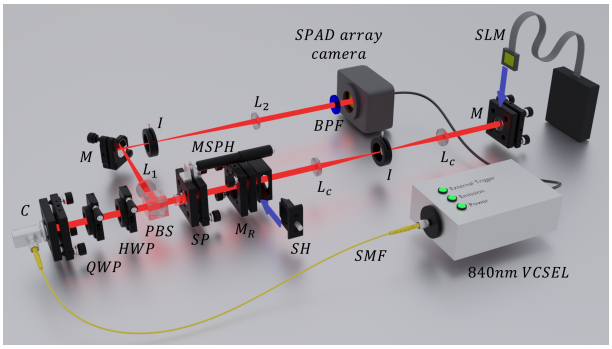

Fig. 3. Experimental Setup. Synchronized light pulses are sent from the VCSEL source into the cavity, while the multiple round outputs are registered in the SPAD array camera. Material samples can be inserted through the sample holder (SH), or simulate by the spatial light modulator (SLM). C: collimator; QWP: quarter-wave plate; HWP: half-wave plate, PBS: polarizing beam splitter; M_R: partially reflective mirror; M: fully reflective mirror; SP: savart plate; MSPH: motorized savart plate holder; I: Iris; L_c: cavity lenses; L_1 and L_2: output telescope lenses; SMF: single-mode fiber; BPF: bandpass filter.

We register the system output with a SPAD array camera, which can recognize every cavity round due to its time-of-flight capabilities. Phase profile estimates are retrieved separately for each round by means of PSDH. Later we combine all phase estimates with the weighting method, according to Eq. (6) and (7). Before performing PSDH, the SP tilting has to be scanned with the cavity optically blocked. Implementing an interpolation similar to Eq. (4) allows to find the motor locations that produce the α_k offsets required by the method.

In order to prevent wrapping effects, we first ensure the direct retrieved phase satisfies the condition $\hat{\theta}^{(n)} < |\pi/2|$. In principle, it is easy to exceed this range with the multi-pass approach after many rounds, but knowing $\hat{\theta}^{(n)} = 2n\hat{\phi}^{(1)}$ as the expected result, one can implement the

Optics EXPRESS

experimental correction $\hat{\phi}^{(n)} = (\hat{\theta}^{(n)} + \hat{\beta}^{(n)})/2n$, with

$$\hat{\beta}^{(n)} = \begin{cases} \frac{-\pi}{n} & \text{if} \quad \hat{\theta}^{(n)} - 2n\hat{\phi}^{(1)} > \pi \\ 0 & \text{if} \quad \left|\hat{\theta}^{(n)} - 2n\hat{\phi}^{(1)}\right| \leq \pi \\ \frac{\pi}{n} & \text{if} \quad \hat{\theta}^{(n)} - 2n\hat{\phi}^{(1)} < -\pi \end{cases} \tag{12}$$

3.2. Image sensor

The SPAD camera we have employed is based on a revised version of the SPAD chip presented in [26], which is designed for single-photon timing and counting. The chip has been manufactured in a 0.16 μm BCD (Bipolar-CMOS-DMOS) SPAD technology and integrates an array of 32 x 32 square SPADs (32 μm × 32 μm) with 100 μm pitch, resulting in a 9.6% fill factor. The photon-detection probability is about 10% at 840 nm and the average dark count rate is 700 cps at 5 V excess bias and room temperature.

The front-end circuit is a gated variable load quenching circuit designed to quickly turn on/off the detectors [27]. With this capability we are able, while triggering the VCSEL with it, to keep the pixels off during a tunable time to prevent detection of the pulse immediately reflected by M_R before entering the cavity. This signal effectively arrives to the SPADs array and could blind it, preventing us to measure large number of rounds. We have experimentally verified that the average duration of the gate rising edge (10-90% transition) is 340 ps.

256 time-to-digital converters, with 204.8 μs full-scale range and 50 ps resolution, are shared among the pixels and a discriminator circuit is employed to preserve the spatial resolution. The complete camera (9×7×5 cm^3) is based on an FPGA and transfers the data to the PC through a USB 3.0 connector allowing frame rates up to 100 kfps. The gate window position can be set with 80 ps precision, in this way the unwanted reflection from the first mirror can be completely filtered out without hiding the first useful peak.

3.3. Data processing steps

Our method requires two acquisition batches, as illustrated in Fig. 4. One batch is recorded with the sample in place and the other without the sample. This way, background information can be removed later. Each batch contains four α-offset acquisitions, with the raw data stored in HDF5 format, where all photon detections are organized using indexes for the frame, timestamp and pixel address. We implement time windows over the counts histogram to extract the number of effective photon detections per round, $p_k^{(n)}(x, y)$. Owing to the acquisition method, the number of frames f per recording might not be identical for all acquisitions in a batch. Therefore, we only consider event counts up to the largest common number of frame f_{max} available in every acquisition of both batches.

The normalization condition shown in Eq. (9) can be implemented by proportionally removing photon counts across all acquisitions of a batch. However, in order to prevent computationally biased effects, we remove frames instead. A new dataset then contains a number of frames described by $f \rightarrow f^{(n)} \approx f \cdot \sum_{x,y} p^{(1)}(x, y)/(\sum_{m=1}^{n} \sum_{x,y} p^{(m)}(x, y))$. Due to statistical fluctuation, the above approximated quantity $f^{(n)}$ is optimized for the best match to the target photon count across the entire SPAD array, $\sum_{m=1}^{n} \sum_{x,y} p'^{(m)}(x, y) = \sum_{x,y} p^{(1)}(x, y)$. Combining phases from different number of rounds n require different normalizations. For this reason, we generated n normalized datasets to fully map the evolution of the phase noise. The subsequent steps are, processing for the phase profiles $\hat{\phi}^{(n)}$ based on Eq. (3), phase unwrapping as in Eq. (12), and phase recombination based on Eq. (6). For the latter, the weighting factors are calculated based on the photon counts across the entire array, $w^{(m)} = m^q \sum_{x,y} p^{(m)}(x, y)/(\sum_{i=1}^{m} \sum_{x,y} i^q p^{(i)}(x, y))$.

Optics EXPRESS

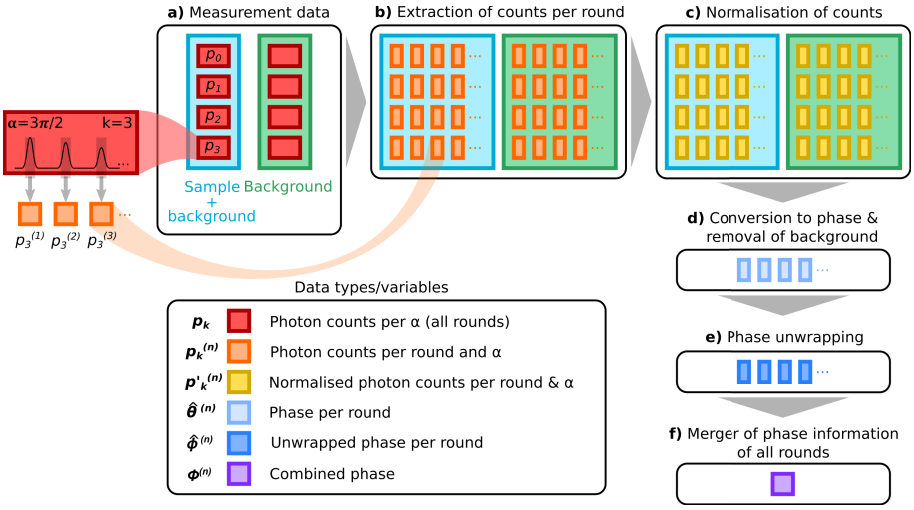

Fig. 4. Workflow diagram. a) Recording of "sample + background" and "background" raw data batches, each with four α-offset acquisitions. b) Photon counts per round are extracted from time windows over the counts histogram. c) New n normalized datasets are produced separately per batch by adjusting the number of frames later utilized. As a result, the number of photon counts across all n rounds equals the number of photon counts in the first round, $\sum_{m=1}^{n}\sum_{x,y} p'^{(m)}(x,y) = \sum_{x,y} p^{(1)}(x,y)$. d) PSDH is implemented following Eq. (3); "sample + background" and "background" are used to obtain the sample phase via removal of the background phase. e) Phase unwrapping is implemented as shown in Eq. (12). f) Phase combination is implemented using Eq. (6).

4. Results

When measuring non-birefringent samples, either in transmission or reflection mode, the method retrieves a sheared phase profile. Alternatively, for birefringent samples, the method can retrieve the "true" phase profile if the SLM retardance axis is aligned with one of the polarizations inside the cavity. In this way, the sample profile is induced in that polarization only, no matter the shear with respect to the other polarization. In our proof of principle we opted for this second case, where the SLM imprints phase only in one of the two polarized beams within the cavity. Accordingly, we can fairly assume the absence of shear in the process ($\tilde{\phi}^{(n)} \equiv \phi^{(n)}$).

In Fig. 5(a) we show a typical histogram of accumulated photon counts, where we implement a 1ns gating around each peak. Working at high time-resolution (50ps per bin) allows us to better remove side peaks which might contain spurious phase profiles, generated for instance from the lenses' back-reflection or even from outer cavity components. In Figs. 5(b), (c) and (d) we show the direct retrieved phase profiles $\hat{\theta}^{(n)}$ for the 2nd, 5th and 8th rounds, respectively. In Figs. 5(e), (f) and (g) we show cross sections of the above profiles, together with the ideal SLM projection and its cross section in (h) and (i), respectively. To better illustrate the increasing values of this retrieved phase we selected a rectangular region of interest (ROI) around the "I" letter in our sample, and from here we extracted the average phase values, which we plot as $\hat{\theta}^{(n)}$ in Fig. 5(j) and $\hat{\phi}^{(n)}$ in Fig. 5(k). Here we see that starting at the 8th round the retrieved phases deviate from the predicted values.

Figure 6 shows how phase measurement sensitivity is enhanced by our method. (a), (c), (e) and (g) show the experimentally retrieved phase profiles $\Phi^{(n)}$ (calculated from Eq. (6) for $n = 1$, $n = 3$, $n = 7$ and $n = 17$ rounds combined, respectively. (b), (d), (f) and (h) show the histogram of pixel-to-pixel differences, $\delta\Phi^{(n)}$, for the rectangular ROI in (a), (c), (e) and (g), respectively.

Optics EXPRESS

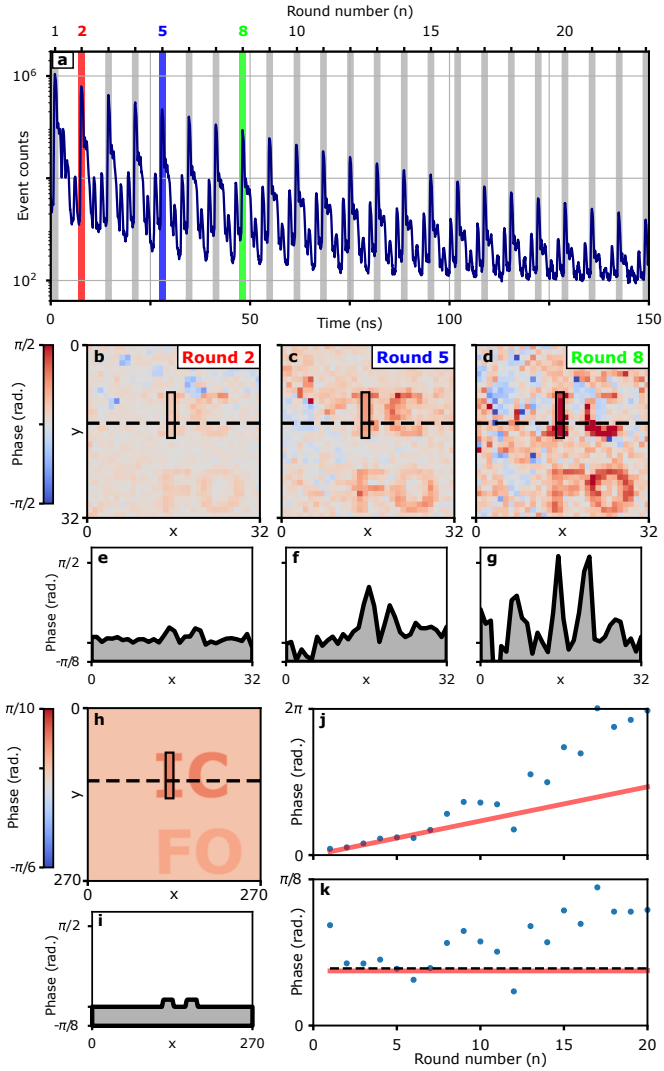

Fig. 5. System calibration results. a) Temporal slicing of the detected pulse train. Direct phase profiles $\hat{\theta}^{(n)}$ for 2nd b), 5th c) and 8th d). e), f) and g) are cross-sections of b), c) and d), respectively. h) is the ideal phase profile, where the I and C (F and O) letters have an expected phase depth of $\phi \approx \pi/21$ ($\phi \approx \pi/42$) over a background level of $\phi = 0$, together with its x-axis cross-section in i). j) Average values of $n\phi^{(n)}$ for the rectangle regions of interest around the letter "I" with a linear prediction in red. k) Average values of $\phi^{(n)}$ for the same regions of interest, with a linear prediction in red.

Optics EXPRESS

This result was obtained with an equal number of total photon detections in all cases. On the left column of Fig. 6 we see that $\Phi^{(7)}$ presents the smoothest profile, because it contains the maximum number of rounds in which $\phi^{(n)}$ does not deviate from the linear prediction, as shown above in Figs. 5(j) and (k). On the right column of Fig. 6 we verify the above since $\delta\Phi^{(7)}$ presents the narrowest distribution. The standard deviation parameter obtained by fitting a Gaussian curve to each $\delta\Phi^{(n)}$ histogram (transparent light blue curves in Fig. 6) yields a quantitative measure of $\Delta\Phi^{(n)}$; this empirical measure of image noise is also known as the local uncertainty (LU) [14,28]. These results were obtained by an absolute number of photons detected equal to $p = 1.109 \cdot 10^7$ among all the four phase-offsets for sample plus background. This was done by accumulating over $f = 62353$ frames, each one with length $t_f = 500\mu$s, giving us a total acquisition time of 31.2s. The four phase-offset acquisitions for background only would require a similar amount of time to collect the same number of photons. The arbitrary photon count rate, to stay under saturation regime, was $3.55 \cdot 10^5$photons$/s$.

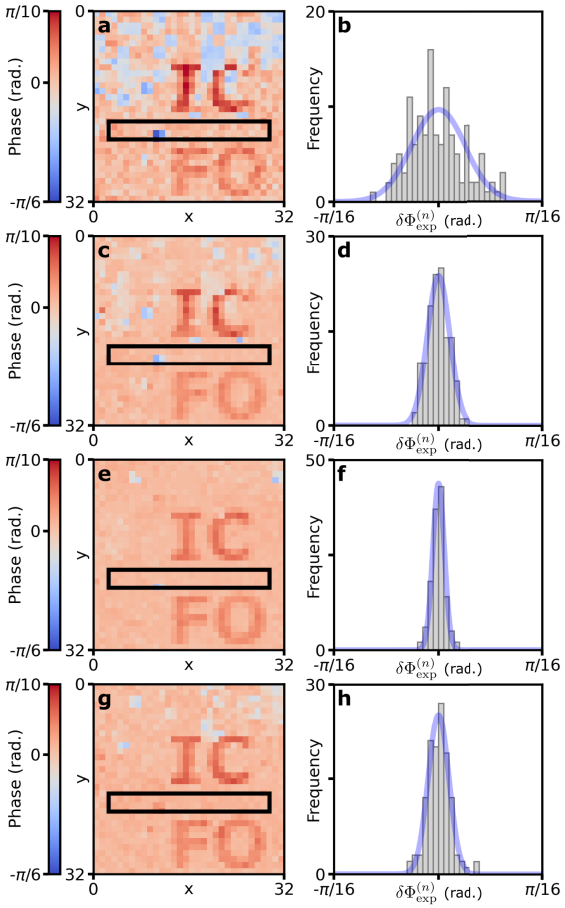

Fig. 6. Multi-pass phase profiles results. Left column: Experimental phase images $\Phi^{(n)}$ retrieved by combining n individual rounds (Eq. (6) and Eq. (7), with $q = 2$). Right column: Histograms of pixel-to-pixel noise in retrieved phase images $\delta\Phi^{(n)}$, i.e., differences between neighbouring pixels in black rectangles in left column; solid blue line: Gaussian fitting. a), b) $n = 1$. c), d) $n = 3$. e), f) $n = 7$. g), h) $n = 17$.

The reduction in experimental phase measurement uncertainty, enabled by our multi-pass combination method, can be quantified by comparing with the single-pass noise $\Delta\Phi^{(1)}$ (i.e.,

Optics EXPRESS

standard deviation of Gaussian fitting function in Fig. 6(b)). Fig. 7 plots the normalized measurement noise $S'(n) \equiv \Delta\Phi^{(n)}/\Delta\Phi^{(1)}$ as a function of n, the number of rounds combined (solid blue line). The grey shaded area represents the statistical standard error in $S'(n)$. As seen in Fig. 7, our method strongly reduces phase measurement uncertainty, approaching closely to the ideal cavity case lower bounded by $1/n$. $\Delta\Phi^{(n)}$ reaches a minimum for $n = 7$, yielding a measurement uncertainty reduction by a factor of 0.22 ± 0.01 compared to the single-pass case $\Delta\Phi^{(1)}$. The absolute phase measurement uncertainty of our method at $n = 7$ is $\Delta\Phi^{(7)} = 0.011 \pm 0.001$rad. For the common phase imaging task of measuring the topography of micro-fabricated silica patterns, the detected phase corresponds to the height of the feature multiplied by the refractive index contrast of $n_1 - n_2 = 0.453$ (more details can be found in [10,29,30]). In this use case therefore our $\Delta\Phi^{(7)}$ corresponds to a depth resolution of 3.3 ± 0.3nm. We also observe in Fig. 7 that for $n \gtrsim 10$ the normalized measurement noise S' increases again. This is attributed to a loss of interference visibility as round number increases, due to imperfect optical alignment causing the probe beam to drift laterally over many rounds. The experimental noise reduction curve $S'(n)$ is consistent with our theoretical model.

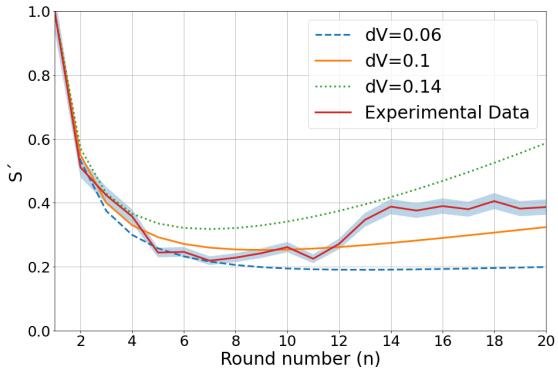

Fig. 7. Phase noise reduction enabled by multipass PSDH. Results evaluated by LU from the selected region of interest shown in Fig. 6. Simulated curves as reference using experimental parameters as $R = 0.05$, $L = 0.05$, $\xi = 0.8$, with $q = 2$ and different values for the visibility decay.

5. Conclusion

Our multi-pass approach combined with PSDH imaging is able to reduce the measurement noise down to 0.22 when compared to the single-pass noise in less than 10 rounds. Theoretically, we can improve this value far beyond, as shown in the Supplement 1, by modifying system parameters like the cavity efficiency, mirror reflectivity and losses, etc. We compared the noise scaling versus other PSDH alternatives, showing how resilient and close to the ideal scenario of no photon decay can be. In order to validate this comparison, the number of photons detected was fixed to a constant number for all experiments. This restriction was implemented computationally by only removing frames from the full dataset, while applying no bias protocols.

We believe the discrepancy between our simulations and the experimental results after round 7 can be explained by a series of factors; i) an increasing influence of the array hot pixels, which have not been deactivated during our tests; ii) the always present dark counts rate and potential cross-talk, which has not been simulated in our model; iii) the Gaussian beam deviation in our 2m full round trip cavity, which prevent photons to always pass through the sample in the same transverse position; iv) the difficulties in the mirrors' alignment in absence of transverse and longitudinal modes interference. We believe that i) and ii) cannot be fully overcome by increasing

Optics EXPRESS

pump power. This choice would produce pixel saturation in very few rounds, then limiting the applicability of the method. With the current components, the cavity size could be reduced by one order of magnitude to make the system more portable and then reduce influence of the beam expansion and deviation, which according to additional results in the Supplement 1, might represent the main source of error in our implementation. Further miniaturization would require an imager with much lower jitter, for instance based on superconducting nanowire single-photon detector arrays, a technology that is not sufficiently mature yet. Lastly, iv) can be overcome by programming the imager FPGA to get live view of the different cavity rounds separately. We consider exploring these improvements in future experimental iterations, as well as theoretical prediction of the sensitivity lower bounds, considering all the above additional restrictions.

One major advantage of the protocol is that it allows large field of view imaging compatible with sample and/or camera scanning, which can increase the (x,y)-resolution as much as the user desires. Additionally, the system can also be used for monitoring fast optical effects (with ns-scale variations) inside the cavity, where our gating mechanism can provide temporal slices of the studied phenomenon. In such a scenario, an nth-gate will have the accumulated information from all previous gates. One can iteratively isolate the nth-gate information only to finally obtain video recordings, as long as the observed phenomenon is optically/electronically triggered in synchronicity with the camera.

Overall, we provide a unique combination of technologies for super-sensitive phase imaging, designed as an optical inspection tool, compatible with reflective and transparent samples with birefringent and/or non-birefringent features. Quantum imaging alternatives, that utilize either multi-photon entanglement or squeezed states of light [31], can provide sensitivities on the same order of magnitude or higher. However, at present such quantum-enhanced approaches are impractical to scale to real-world advantages, due to demanding experimental requirements such as very high optical efficiencies.

Funding. Agència de Gestió d'Ajuts Universitaris i de Recerca (2021 SGR 01458); H2020 Marie Skłodowska-Curie Actions (713729 (ICFOstepstone 2)); H2020 Future and Emerging Technologies (801060 (Q-MIC))); Generalitat de Catalunya; Centres de Recerca de Catalunya; FUNDACIÓ Privada MIR-PUIG; Fundación Cellex; Agencia Estatal de Investigación (CEX2019-000910-S, MCIN/AEI/10.13039/501100011033, PID2019-106892RB-I00); European Union Next Generation (PRTR-C17.I1).

Acknowledgments. This study was supported by MICIIN with funding from European Union NextGenerationEU (PRTR-C17.I1) and by Generalitat de Catalunya.

Disclosures. The authors declare no conflicts of interest.

Data availability. Data underlying the results presented in this paper are not publicly available at this time but may be obtained from the authors upon reasonable request.

Supplemental document. See Supplement 1 for supporting content.

References

1. B. L. Higgins, D. W. Berry, S. D. Bartlett, H. M. Wiseman, and G. J. Pryde, "Entanglement-free heisenberg-limited phase estimation," Nature **450**(7168), 393–396 (2007).
2. V. Giovannetti, S. Lloyd, and L. Maccone, "Quantum-Enhanced Measurements: Beating the Standard Quantum Limit," Science **306**(5700), 1330–1336 (2004).
3. E. Fuentes-Lemus and C. López-Alarcón, "Photo-induced protein oxidation: mechanisms, consequences and medical applications," Essays Biochem. **64**(1), 33–44 (2020).
4. D. I. Pattison, A. S. Rahmanto, and M. J. Davies, "Photo-oxidation of proteins," Photochem. & Photobiol. Sci. **11**(1), 38–53 (2012).
5. G. Popescu, *Quantitative Phase Imaging of Cells and Tissues* (McGraw-Hill Education, New York, 2011), 1st ed.
6. W. Zhang, Y. Ye, Y. Hu, K. Li, and C. Liu, "Photo-induced structural and optical changes of cspbbr3 perovskite nanocrystals in glasses," Chem. Eng. J. **454**, 140142 (2023).
7. W. Lang and others, *Nomarski differential interference-contrast microscopy* (Carl Zeiss Oberkochen, 1982).
8. D. Gabor, "A New Microscopic Principle," Nature **161**(4098), 777–778 (1948).
9. D. Malacara, *Optical shop testing, Wiley series in pure and applied optics* (Wiley, Hoboken, N.J, 2007), 3rd ed.
10. R. A. Terborg, J. Pello, I. Mannelli, J. P. Torres, and V. Pruneri, "Ultrasensitive interferometric on-chip microscopy of transparent objects," Sci. Adv. **2**(6), e1600077 (2016).

Optics EXPRESS

11. X. Chen, M. E. Kandel, S. He, C. Hu, Y. J. Lee, K. Sullivan, G. Tracy, H. J. Chung, H. J. Kong, M. Anastasio, and G. Popescu, "Artificial confocal microscopy for deep label-free imaging," Nat. Photonics **17**(3), 250–258 (2023).
12. R. Juskaitis, T. Wilson, and N. Rea, "Compact confocal interference microscopy," Opt. Commun. **109**(1-2), 167–177 (1994).
13. S. Haegele, G. Corrielli, M. Hejda, L. Duempelmann, R. A. Terborg, R. Osellame, and V. Pruneri, "Large field-of-view holographic imager with ultra-high phase sensitivity using multi-angle illumination," Opt. Lasers Eng. **161**, 107315 (2023).
14. R. Camphausen, Álvaro Cuevas, L. Duempelmann, R. A. Terborg, E. Wajs, S. Tisa, A. Ruggeri, I. Cusini, F. Steinlechner, and V. Pruneri, "A quantum-enhanced wide-field phase imager," Sci. Adv. **7**(47), eabj2155 (2021).
15. T. Juffmann, B. B. Klopfer, T. L. I. Frankort, P. Haslinger, and M. A. Kasevich, "Multi-pass microscopy," Nat. Commun. **7**(1), 12858 (2016).
16. Y. Israel, J. L. Reynolds, B. B. Klopfer, and M. A. Kasevich, "Continuous wave multi-pass imaging flow cytometry," Optica **10**(4), 491–496 (2023).
17. A. J. Bowman, B. B. Klopfer, T. Juffmann, and M. A. Kasevich, "Electro-optic imaging enables efficient wide-field fluorescence lifetime microscopy," Nat. Commun. **10**(1), 1–8 (2019).
18. D. Wildanger, E. Rittweger, L. Kastrup, and S. W. Hell, "Sted microscopy with a supercontinuum laser source," Opt. Express **16**(13), 9614–9621 (2008).
19. Y. Wu, X. Wu, R. Lu, J. Zhang, L. Toro, and E. Stefani, "Resonant scanning with large field of view reduces photobleaching and enhances fluorescence yield in sted microscopy," Sci Rep **5**(1), 14766 (2015).
20. B. O. Leung and K. C. Chou, "Review of super-resolution fluorescence microscopy for biology," Appl. Spectrosc. **65**(9), 967–980 (2011).
21. M. J. Rust, M. Bates, and X. Zhuang, "Sub-diffraction-limit imaging by stochastic optical reconstruction microscopy (storm)," Nat. Methods **3**(10), 793–796 (2006).
22. R. Demkowicz-Dobrzanski, "Multi-pass classical vs. quantum strategies in lossy phase estimation," Laser Phys. **20**(5), 1197–1202 (2010).
23. A. J. Bowman, B. B. Klopfer, T. Juffmann, and M. A. Kasevich, "Electro-optic imaging enables efficient wide-field fluorescence lifetime microscopy," Nat. Commun **10**(1), 4561 (2019).
24. K. Sharma, D. Venkitesh, and S. Bhattacharya, "Enhanced sensitivity in cavity ring down spectroscopy using q-switched fiber lasers," in *Workshop on Recent Advances in Photonics (WRAP)*, (2013), pp. 1–2.
25. A. Maity, S. Maithani, and M. Pradhan, "Cavity ring-down spectroscopy: Recent technological advancements, techniques, and applications," Anal. Chem. **93**(1), 388–416 (2021).
26. D. Portaluppi, E. Conca, and F. Villa, "32 × 32 cmos spad imager for gated imaging, photon timing, and photon coincidence," IEEE J. Sel. Top. Quantum Electron. **24**(2), 1–6 (2018).
27. S. Tisa, F. Zappa, A. Tosi, and S. Cova, "Electronics for single photon avalanche diode arrays," Sensors Actuators A: Phys. **140**(1), 113–122 (2007).
28. Y. Israel, S. Rosen, and Y. Silberberg, "Supersensitive polarization microscopy using noon states of light," Phys. Rev. Lett. **112**(10), 103604 (2014).
29. 'www.refractiveindex.info,'.
30. R. Camphausen, A. S. Perna, Álvaro Cuevas, A. Demuth, J. A. Chillón, M. Gräfe, F. Steinlechner, and V. Pruneri, "Fast quantum-enhanced imaging with visible-wavelength entangled photons," Opt. Express **31**(4), 6039–6050 (2023).
31. C. A. Casacio, L. S. Madsen, A. Terrasson, M. Waleed, K. Barnscheidt, B. Hage, M. A. Taylor, and W. P. Bowen, "Quantum-enhanced nonlinear microscopy," Nature **594**(7682), 201–206 (2021).